I&EC research
Industrial & Engineering Chemistry Research

Article

pubs.acs.org/IECR

Poly(ionic liquid)-Based Nanocomposites and Their Performance in CO_2 Capture

Hua Cheng,[†,‡] Ping Wang,[‡,§] Jiangshui Luo,[∥] Jan Fransaer,[⊥] Dirk E. De Vos,[∥] and Zheng-Hong Luo*[,§,#]

[†]School of Chemistry and Chemical Engineering, Hefei Normal University, Hefei 230061, P. R. China

[§]Department of Chemical and Biochemical Engineering, College of Chemistry and Chemical Engineering, Xiamen University, Xiamen 361005, P. R. China

[#]Department of Chemical Engineering, School of Chemistry and Chemical Engineering, Shanghai Jiao Tong University, Shanghai 200240, P. R. China

[∥]Centre for Surface Chemistry and Catalysis and [⊥]Department of Materials Engineering, KU Leuven, Leuven 3001, Belgium

ABSTRACT: To search for robust CO_2 capture materials, two types of ionic liquids, namely, (*p*-vinylbenzyl)-trimethylammonium tetrafluoroborate ([VBTMA][BF_4]) and (*p*-vinylbenzyl)trimethylammonium hexafluorophosphate ([VBTMA][PF_6]), were synthesized and immobilized onto a mesoporous silica (meso-silica) support by the surface-initiated atom-transfer radical polymerization (SI-ATRP) method. The prepared sorbents meso-SiO_2−P[VBTMA][BF_4] and meso-SiO_2−P[VBTMA][PF_6] were well-characterized. Their adsorption behaviors toward CO_2 from simulated flue gases at different pressures were investigated using an adsorption column. Based on a simulated flue gas containing 10 vol % CO_2 at 30 °C, the highest CO_2 adsorption capacity of meso-SiO_2−P[VBTMA][BF_4] was 0.4025 mmol g^{-1}, whereas the corresponding value for meso-SiO_2−P[VBTMA][PF_6] was 0.3793 mmol g^{-1}. Compared with pure poly(ionic liquid)s, the existence of a meso-silica core improves the CO_2 capture capacity. Furthermore, the presence of vapor can improve the CO_2 capture capacity. However, an increase in temperature inhibits the CO_2 capture capacity, implying that the nanocomposites should preferably be used at low temperature.

■ INTRODUCTION

Currently, the effects of increasing atmospheric carbon dioxide (CO_2) concentrations, which lead to global climate change, have attracted growing attention from researchers worldwide. Not only is the application of CO_2 capture important for environmental issues, but also the removal of CO_2 from gas streams is necessary for some other application areas such as air purification in confined spaces[1,2] and natural gas treatment.[3−5] To help achieve the goal of decreasing CO_2 emissions, the synthesis of more efficient organically functionalized materials as CO_2 capture agents has received considerable attention.[6]

Ionic liquids are a type of organic salts that have low melting points[7,8] and outstanding CO_2 solubilities.[9−12] Such materials are often utilized as nonvolatile and regenerable carbon dioxide absorbents. Furthermore, they can be grafted onto porous materials to prepare supported liquid membranes.[13,14] Ionic liquids can endow polymer backbones with ion conducting groups, giving rise to polymers with great stability that can be widely used in material science.[15−21] In 2005, Tang et al. found that the absorption ability of poly(ionic liquid)s for CO_2 is stronger than that of the corresponding monomers for the first time. According to the published literature, ammonium-based poly(ionic liquid)s have stronger CO_2 absorption abilities than imidazolium-based poly(ionic liquid)s.[22] Moreover, when poly(ionic liquid)s bond with other anions, their hydrated membranes exhibit high gas permeabilities and remarkable selectivities,[23−27] which is useful for gas separation. However, the capacity is still poor, and the high cost of poly(ionic liquid)s restricts their development. Compared with poly(ionic liquid)s, traditional absorbents such as mesoporous materials have relatively high capacities but not excellent selectivities. Therefore, it would be a significant improvement if poly(ionic liquid)s could be successfully synthesized on the surface of mesoporous particles.

To modify and functionalize the surfaces of composites, surface-initiated controlled radical polymerization (SI-CRP) could serve as an effective method in the synthesis process. Because the SI-CRP process involves rapid initiation but slow growth of the polymer chains, it is helpful to guarantee a high grafting density and uniform polymer chains.[28−41] Among CRP methods, atom-transfer radical polymerization (ATRP) is a promising and effective method, because it can operate under simple conditions and is suitable for numerous types of monomers. In surface-initiated ATRP, all of the initiator moieties can be immobilized on the surface, so that every polymer chain can form a strong bond with the surface. The published literature indicates that many types of of monomers (methacrylate, styrene, etc.[29−32]) can be grafted successfully by surface-initiated ATRP.

In this work, two types of ionic liquids, namely, (*p*-vinylbenzyl)trimethylammonium tetrafluoroborate ([VBTMA]-[BF_4]) and (*p*-vinylbenzyl)trimethylammonium hexafluorophosphate ([VBTMA][PF_6]), were synthesized and grafted onto a mesoporous silica (meso-silica) support by the SI-ATRP method. Meso-SiO_2−P[VBTMA][BF_4] and meso-SiO_2−P-

Received: December 25, 2014
Revised: March 8, 2015
Accepted: March 18, 2015
Published: March 18, 2015

DOI: 10.1021/ie505014h
Ind. Eng. Chem. Res. 2015, 54, 3107−3115

Scheme 1. Synthesis Route for the Two Nanocomposite Adsorbents by SI-ATRP

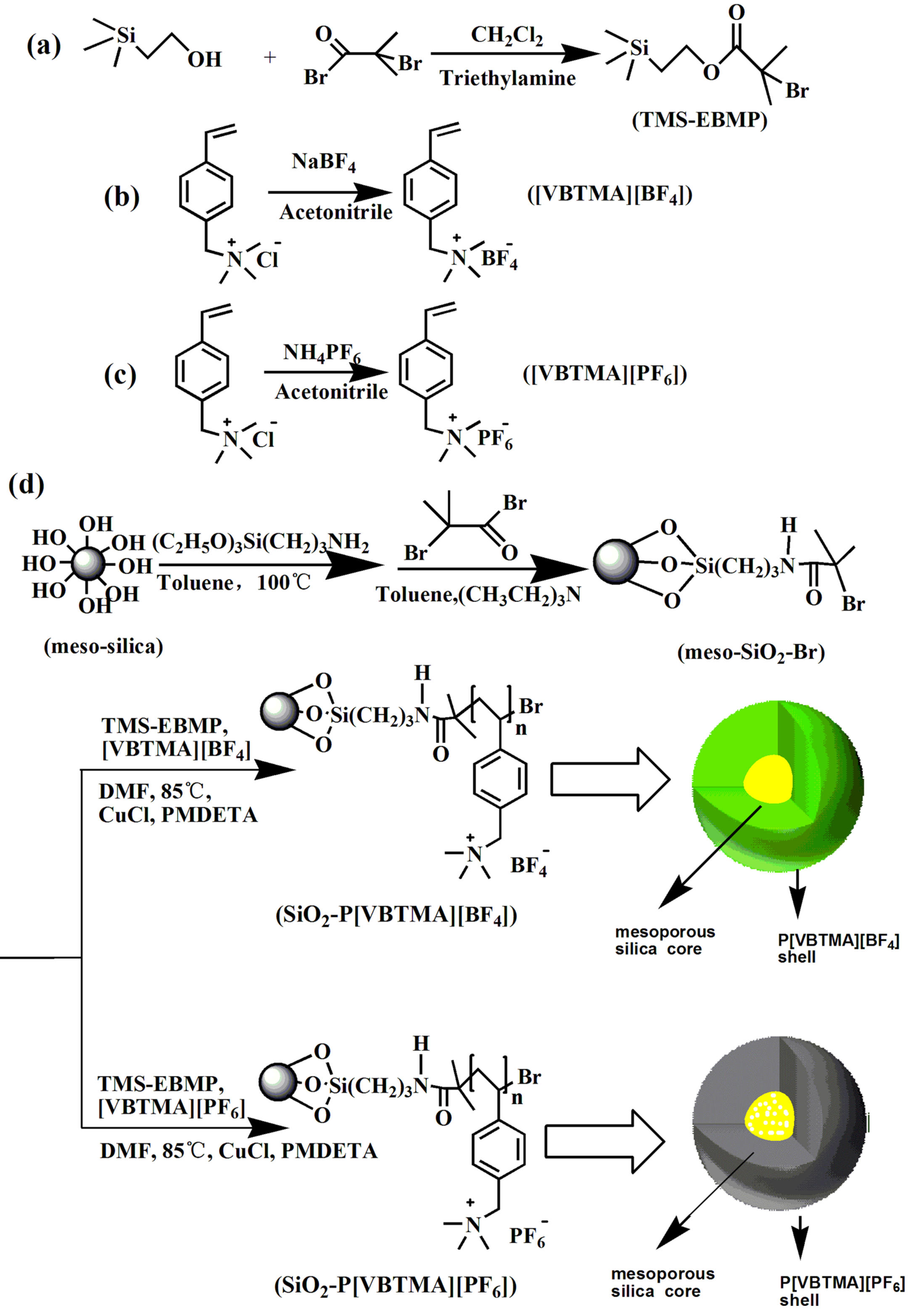

[VBTMA][PF_6] were first characterized using ^1H nuclear magnetic resonance (NMR) spectroscopy, Fourier transform infrared (FT-IR) spectroscopy, thermogravimetric analysis (TGA), and scanning electron microscopy (SEM). Subsequently, the CO_2 capture capacities of meso-SiO_2−P-[VBTMA][BF_4] and meso-SiO_2−P[VBTMA][PF_6] were examined systematically. In addition, four factors influencing CO_2 capture capacity were investigated. The developed poly(ionic liquid)-based nanocomposites are promising for CO_2 capture.

■ EXPERIMENTAL SECTION

Materials. Mesoporous nanosilica (mean size, 7.6 nm; pore volume, 1.28 $cm^3 \cdot g^{-1}$; surface area, 336 $m^2 \cdot g^{-1}$) was dried at 110 °C under a vacuum overnight before use. CuCl [99%, Sinopharm Chemical Reagent Co., Ltd. (SCRC)] was purified by acetic acid and methanol and dried at 45 °C under a vacuum. (*p*-Vinylbenzyl)trimethylammonium chloride ([VBTMA][Cl]; 99%, Sigma-Aldrich), *N*,*N*,*N*′,*N*″,*N*″-pentamethyl diethylenetriamine (PMDETA; 98%, Sigma-Aldrich), 3-aminopropyltriethoxysilane (APTES; 98%, Alfa Asar), 2-bromoisobutyryl bromide (BiBB; 98%, Alfa Asar), sodium tetrafluoroborate ($NaBF_4$; 99%, Aladdin), ammonium hexafluorophosphate (NH_4PF_6; 98%, Aladdin), and 2-(trimethylsilyl)ethanol (99%, Aladdin) were used as received. Other materials were used as received from SCRC without further purification.

Synthesis of TMS-EBMP. The detailed preparation of 2-(trimethylsilyl)ethyl 2-bromo-2-methylpropanoate (TMS-EBMP) can be found in our previous publication,[42] and the reaction process is shown in Scheme 1a.

Synthesis of [VBTMA][BF_4] and [VBTMA][PF_6]. [VBTMA][BF_4] was prepared according to the published method,[42] as shown in Scheme 1b. [VBTMA][PF_6] was prepared using ammonium halide by an ion-exchange reaction, as shown in Scheme 1c. First, CH_3CN (15 mL), NH_4PF_6 (2.15 g, 0.0132 mol), and [VBTMA][Cl] (2.54 g, 0.012 mol) were placed in a flask. Then, similarly to the synthesis of [VBTMA][BF_4], white crystals of [VBTMA][PF_6] were obtained prior to cryopreservation under sealed conditions. ^1H NMR for [VBTMA][PF_6]: δ 3.02 (s, 9H), 4.50 (s, 2H), 5.38 (d, 1H), 5.96 (d, 1H), 6.81 (q, 1H), 7.50(d, 2H), 7.61 (d, 2H). M_n: 321.8 g·mol^{-1}. Melting point: 171−175 °C.

Synthesis of *meso*-SiO_2−P[VBTMA][BF_4] and *meso*-SiO_2−P[VBTMA][PF_6] Nanocomposites. The synthesis process for meso-SiO_2−Br was the same as in our previous work[42] ([meso-SiO_2−Br] = 3.57×10^{-8} mol·dm^{-2}, specific surface area of meso-SiO_2 = 336 m^2·g^{-1}). At a [monomer]/[initiator]/[CuCl]/[PMDETA] ratio of 100:1:1:1, initiator-immobilized meso-silica particles, [VBTMA][BF_4] (2.634 g, 10.0 mmol), and dimethylformamide (DMF; 4.0 mL) were added to a flask, followed by CuCl (9.9 mg, 0.1 mmol) and PMDETA (20.8 μL, 0.1 mmol). After the system had been degassed, TMS-EBMP (13.4 mg, 0.05 mmol) was injected to start the reaction. After a desired reaction time at 85 °C, the reaction was stopped, and SiO_2−P[VBTMA][BF_4] was obtained through centrifugation. To eliminate physically absorbed polymer chains, the SiO_2−P[VBTMA][BF_4] was washed with DMF several times and dried at 70 °C under a vacuum. The supernatant was evaporated, and the resultant product was precipitated using cold methanol/water (volume ratio = 4:1) and dried under a vacuum at 45 °C. The synthesis process for meso-SiO_2−P[VBTMA][PF_6] nanocomposites was the same as that for meso-SiO_2−P[VBTMA][BF_4] nanocomposites (Scheme 1d).

Measurements. ^1H nuclear magnetic resonance spectra were measured using a Bruker Advance II 400 MHz instrument and deuterated dimethyl sulfoxide (DMSO-d_6) as the solvent.

Melting points were detected on a X-4 digital display microscopic melting point meter calibrated by acetanilide (melting point = 114 °C).

Fourier transform infrared (FT-IR) spectra were recorded using Nicolet Avatar 330 FT-IR spectrophotometer in transmittance mode.

Elemental analysis (EA) was performed on a Vario EL III elemental analyzer.

X-ray photoelectron spectroscopy (XPS) analysis was carried out using a PHI Quantum 2000 scanning electron spectroscopy for chemical analysis (ESCA) microprobe. The exciting source was Al Kα_{12} radiation with a binding energy of 1486.60 eV and a voltage of 15 kV in constant-analyzer-energy (CAE) mode, and the energy was calibrated at C 1s = 284.8 eV.

Thermogravimetric analysis (TGA) was performed on an SDTQ 600 instrument from room temperature to 800 °C under a nitrogen atmosphere at a 10 °C·min^{-1} heating rate.

Scanning electron microscopy (SEM) observations were made on a Hitachi S-4800 microscope at an acceleration voltage of 10 kV. The samples were prepared as follows: A 0.2 mg·mL^{-1} ethanol solution of meso-silica and meso-SiO_2−Br and a 0.2 mg·mL^{-1} DMF solution of meso-SiO_2−P[VBTMA][BF_4] and meso-SiO_2−P[VBTMA][PF_6] were mounted onto silicon wafers and dried at room temperature.

The CO_2 capture capacity was measured on a CO_2 adsorption system that mainly consisted of adsorbed gas, purge gas, fixed adsorber, flow and pressure regulating system, and a gas concentration analysis system (Scheme 2). The adsorption column filled with 1.5 g of adsorbent was placed in a temperature-controlled tubular furnace. CO_2 was blended with nitrogen (99.99%). Gas chromatography (GC) was used to detect the CO_2 concentration. Adsorbents were treated under a nitrogen flow of 50 mL·min^{-1} at 150 °C for 90 min and then cooled to 30 °C. After that, the nitrogen flow was switched to a CO_2-containing simulated flue gas at 50 cm^3·min^{-1}, which kept the mole fraction of CO_2 at 0.1 at atmospheric pressure.

Scheme 2. Schematic Drawing of the CO_2 Adsorption Experimental System[a]

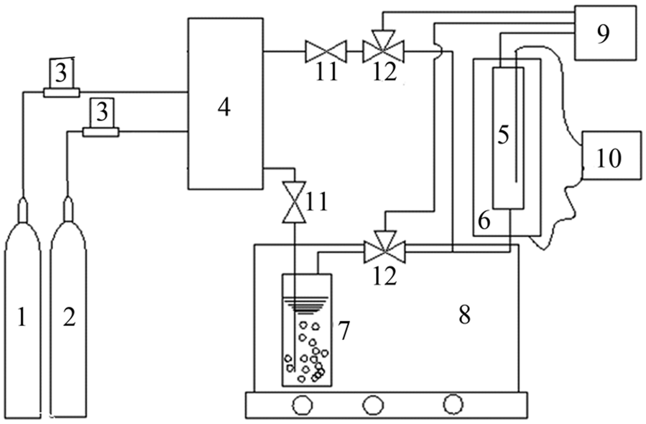

[a]Components: (1) nitrogen, (2) carbon dioxide, (3) mass spectrometer, (4) mixture tank, (5) adsorption column, (6) tubular furnace, (7) saturator, (8) water bath, (9) gas chromatograph, (10) temperature controller, (11) ball valve, (12) three-way ball valve.

■ RESULTS AND DISCUSSION

Characterization of SiO_2−P[VBTMA][BF_4] and SiO_2−P[VBTMA][PF_6] Nanocomposites. Using the trimethylsilyl-(TMS-) labeled "sacrificial initiator" method, the obtained macromolecules in solution served as a reference substance for the polymers formed on the surface. Thus, the molecular weight and polydispersity of the grafted polymer could be analyzed by size-exclusion chromatography (SEC) of the polymer obtained in solution. However, because the charged groups existing in the polyionic material could lead to a complicated and unreliable molecular weight, it is difficult to characterize such materials by SEC. Herein, the monomer conversion was obtained through a gravimetric method, and the number-average molecular weights ($M_{n,NMR}$) of the precipitated TMS–P[VBTMA][BF_4] and TMS–P[VBTMA][PF_6] were calculated from ^{1}H NMR spectra by the trimethylsilyl-(TMS-) labeled sacrificial initiator method. The detailed calculation process was presented in our previous work.[42] The ^{1}H NMR spectra of the resultant polymers and the kinetics of ATRP are shown in Figure 1. As depicted in Figure 1a, the two signals present at 7.1 and 6.5 ppm correspond to the benzene ring group. The signal at 4.3 ppm is attributed to methylene belonging to a benzene ring. The signal at 2.9 ppm corresponds to methyl groups attached to a nitrogen atom. The broad peak at 1.5 ppm originates from the methene and methine protons of the main chain. The characteristic signal of TMS-labeled initiator is located at 0.0 ppm and was used to calculate the degree of polymerization. In addition, the linearity of the kinetic plot (Figure 1b) demonstrates the constant number of active species in the two systems. At the end of polymerization, the conversions of the [VBTMA][BF_4] and [VBTMA][PF_6] systems were about 53% and 54%, respectively. Clearly, the two monomers have similar polymerization rates. The evolution of $M_{n,NMR}$ (Figure 1c) also increased linearly as polymerization proceeded, and the two poly(ionic liquid)s had similar degrees of polymerization after predetermined polymerization times (Figure 1b). Because of the different molecular weights of the monomers, M_n for TMS–P[VBTMA][PF_6] was 17775 g·mol^{-1}, and M_n for TMS–P[VBTMA][BF_4] was 14378 g·mol^{-1}. These results demonstrate the classical features of ATRP.

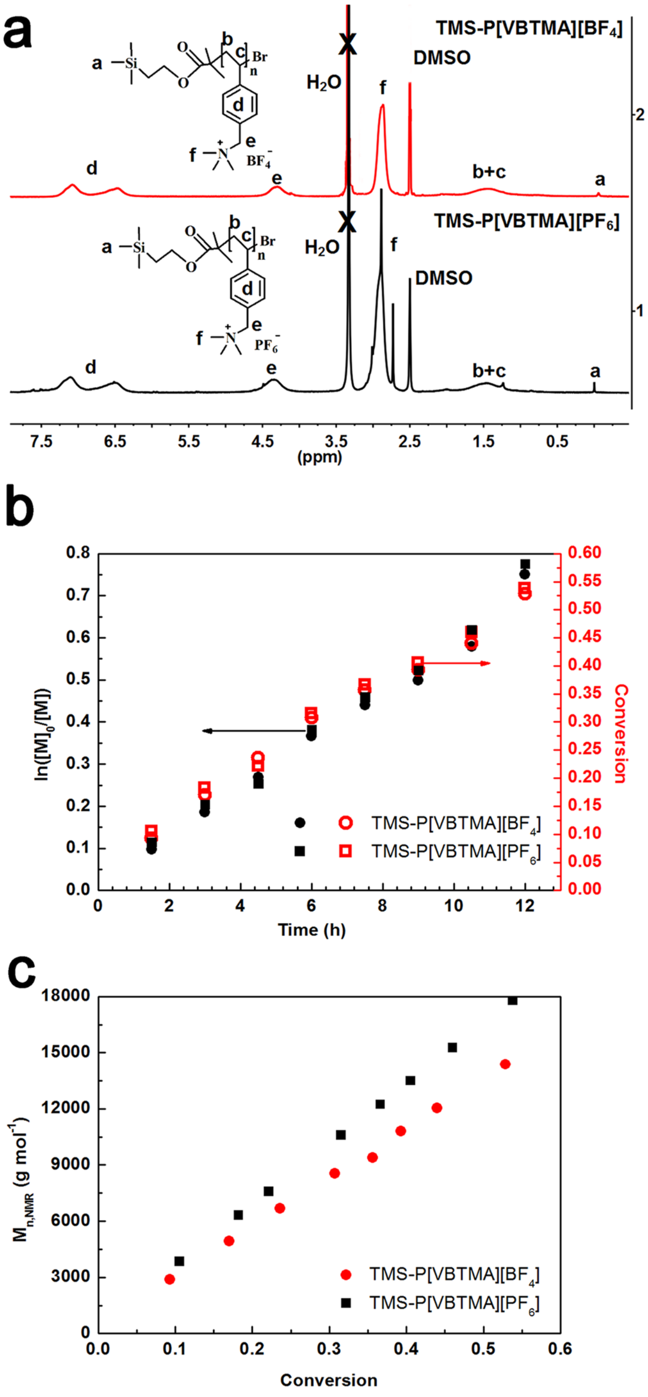

Figure 1. Experimental data for TMS–P[VBTMA][BF_4] and TMS–P[VBTMA][PF_6]: (a) ^{1}H NMR spectra, (b) semilogarithmic kinetic plot and monomer conversion vs polymerization time, (c) molecular weight ($M_{n,\ NMR}$) vs monomer conversion.

Core–shell meso-SiO_2–P[VBTMA][BF_4] and meso-SiO_2–P[VBTMA][PF_6] were synthesized by SI-ATRP (Scheme 1d). The FT-IR spectra of the products are presented in Figure 2.

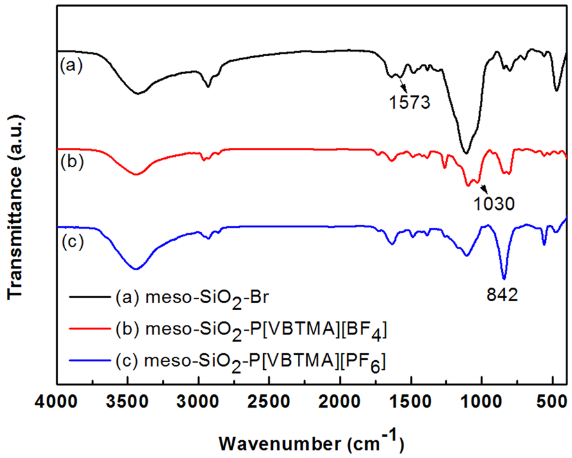

Figure 2. FT-IR spectra of (a) meso-SiO_2–Br, (b) meso-SiO_2–P[VBTMA][BF_4], and (c) meso-SiO_2–P[VBTMA][PF_6].

For meso-SiO_2–Br (Figure 2a), the signals at 1109 and 470 cm^{-1} originated from tetrahedral silica structures. The signal for Si–O–Si bending can be found at 800 cm^{-1}. In addition, the presence of amide groups (N–H bending) could be verified by the peak at 1573 cm^{-1}. The CH_3 stretching and bending vibration was confirmed by signals at 1383 and 2931 cm^{-1}. In the FT-IR spectrum of meso-SiO_2–P[VBTMA][BF_4] (Figure 2b), the characteristic peaks of both the meso-SiO_2 core and the P[VBTMA][BF_4] shell are included. The peaks for C–H bending vibration are located at 807 and 841 cm^{-1}, whereas that for the benzene ring in P[VBTMA][BF_4] is located at 1418 and 1485 cm^{-1}. In particular, the peak at 1030 cm^{-1} belonging to B–F stretching vibrations indicates that the surface of the nanosilica particles was successfully grafted with P[VBTMA][BF_4]. Similarly, in the FT-IR spectrum of meso-SiO_2–P[VBTMA][PF_6] (Figure 2c), characteristic peaks were also observed, and the signal for the P–F stretching vibration at 842 cm^{-1} verified that P[VBTMA][PF_6] was also successfully grafted.

Additionally, the elemental contents of meso-SiO_2−P[VBTMA][BF_4] and meso-SiO_2−P[VBTMA][PF_6] were obtained by EA as summarized in Table 1. For meso-SiO_2−P[VBTMA][BF_4], the EA data show the following contents: N, 4.99%; H, 6.69%; C, 51.53%. The values calculated from the molecular formula of the corresponding monomer [VBTMA][BF4] are N, 5.32%; H, 6.90%; C, 54.78%. For meso-SiO_2−P[VBTMA][PF_6], the EA data indicate the following contents: N, 4.42%; H, 5.54%; C, 42.32%. The values calculated from the molecular formula of [VBTMA][PF6] are N, 4.36%; H, 5.65%; C, 44.87%. Generally speaking, the elemental contents in the nanocomposites decreased only slightly in comparison to those in the monomer, which might be the result of the immobilization of the initiator onto meso-SiO_2 in the nanocomposite. Furthermore, the uncertainty during testing and software measurement deviations could also cause differences, which might be the reason the EA value is much greater than the calculated value for the N content in meso-SiO_2−P[VBTMA][PF_6]. However, the deviations of all the detected elemental contents were within the error allowance, and the data still indicate that the SI-ATRP was successful.

Table 1. EA and Calculated Elemental Contents

material	C (%)	H (%)	N (%)
meso-SiO_2−P[VBTMA][BF_4][a]	51.53	6.69	4.99
[VBTMA][BF_4][b]	54.78	6.90	5.32
meso-SiO_2−P[VBTMA][PF_6][a]	42.32	5.54	4.42
[VBTMA][PF_6][b]	44.87	5.65	4.36

[a] Average of two EA results. [b] Calculated from the corresponding molecular formula.

XPS spectra were also obtained to verify the successful immobilization of P[VBTMA][BF_4] and P[VBTMA][PF_6]. The F 1s, N 1s, and B 1s spectra of the meso-SiO_2−P[VBTMA][BF_4] surface are shown in Figure 3 to confirm the structure. In Figure 3b, the F 1s, N 1s, and B 1s signals are located at 686.0, 402.6, and 194.1 eV, respectively. The N 1s peak at 402.6 eV belongs to the nitrogen atom (N^+) of the [VBTMA] cation. The XPS survey spectra of F 1s (686.5 eV), N 1s (402.6 eV), and P 2p (136.6 eV) for the P[VBTMA][PF_6] shell on the silica surface can be found in Figure 4.

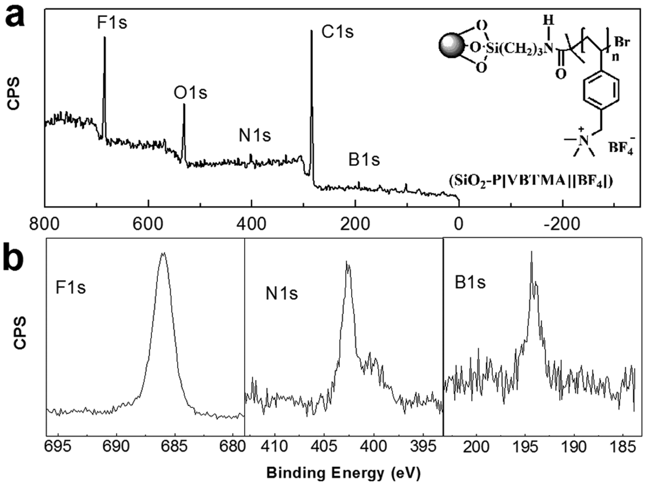

Figure 3. (a) XPS survey spectrum and (b) high-resolution F 1s, N 1s, and B 1s elemental scans of the meso-SiO_2−P[VBTMA][BF_4] surface.

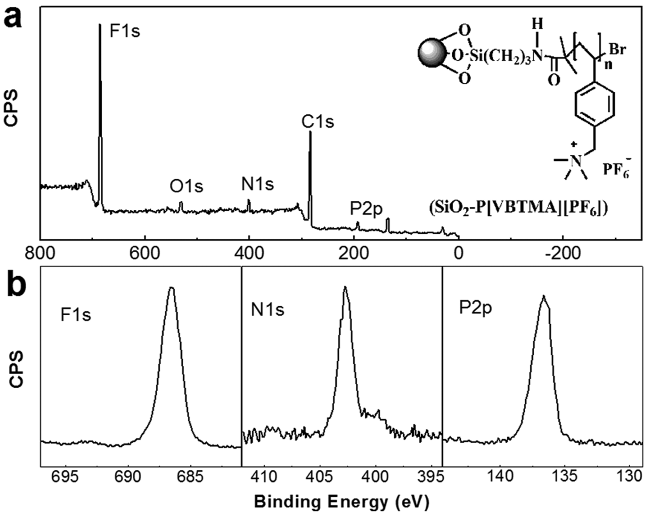

Figure 4. (a) XPS survey spectrum and (b) high-resolution F 1s, N 1s, and P 2p elemental scan of the meso-SiO_2−P[VBTMA][PF_6] surface.

Thermal Properties. The TGA curves of meso-SiO_2−Br, meso-SiO_2−P[VBTMA][BF_4], and meso-SiO_2−P[VBTMA][PF_6] are displayed in Figure 5. Corresponding to its higher M_n value, meso-SiO_2−P[VBTMA][PF_6] has a higher weight loss than meso-SiO_2−P[VBTMA][BF_4] involving similar monomer units, which is caused by the cleavage of the polymer backbone, namely, carbonation. The organic components present in the products result in the weight losses shown in the TGA curves of meso-SiO_2−Br, meso-SiO_2−P[VBTMA][BF_4], and meso-SiO_2−P[VBTMA][PF_6]. Before thermal decomposition, there is a small quantity of weight loss in the three curves, which might be because of the evaporation of physically adsorbed water. Because of the greater hydrophilicity of the P[VBTMA][BF_4] shell, this phenomenon was much more obvious for meso-SiO_2−P[VBTMA][BF_4]. It can be seen that the residual weights for meso-SiO_2−P[VBTMA][BF_4] and meso-SiO_2−P[VBTMA][PF_6] were 25.6% and 13.0%, respectively, at 750 °C. The decomposition temperatures of meso-SiO_2−P[VBTMA][BF_4] and meso-SiO_2−P[VBTMA][PF_6] both exceed 300 °C, implying that they both exhibit excellent thermal stability.

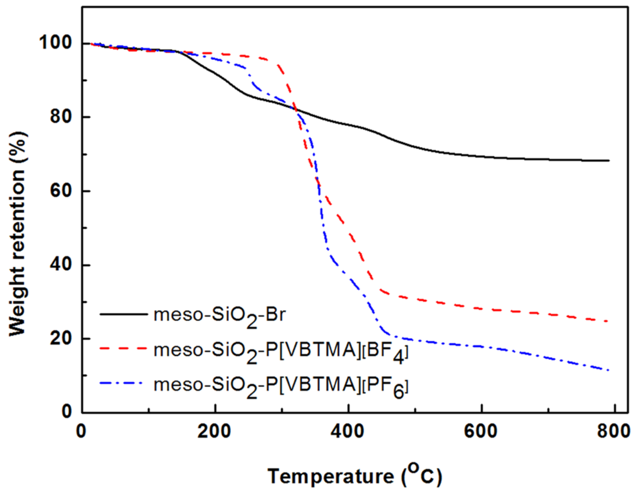

Figure 5. TGA curves of (a) meso-SiO_2−Br, (b) meso-SiO_2−P[VBTMA][BF_4], and (c) meso-SiO_2−P[VBTMA][PF_6].

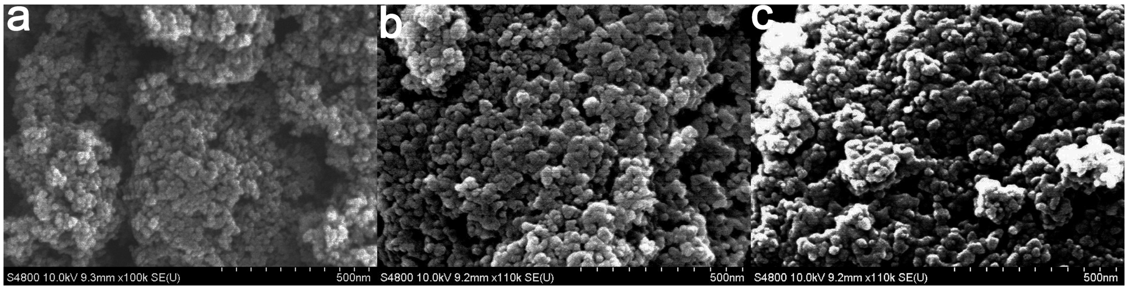

Figure 6. SEM images of (a) meso-SiO_2−Br, (b) meso-SiO_2−P[VBTMA][BF_4], and (c) meso-SiO_2−P[VBTMA][PF_6].

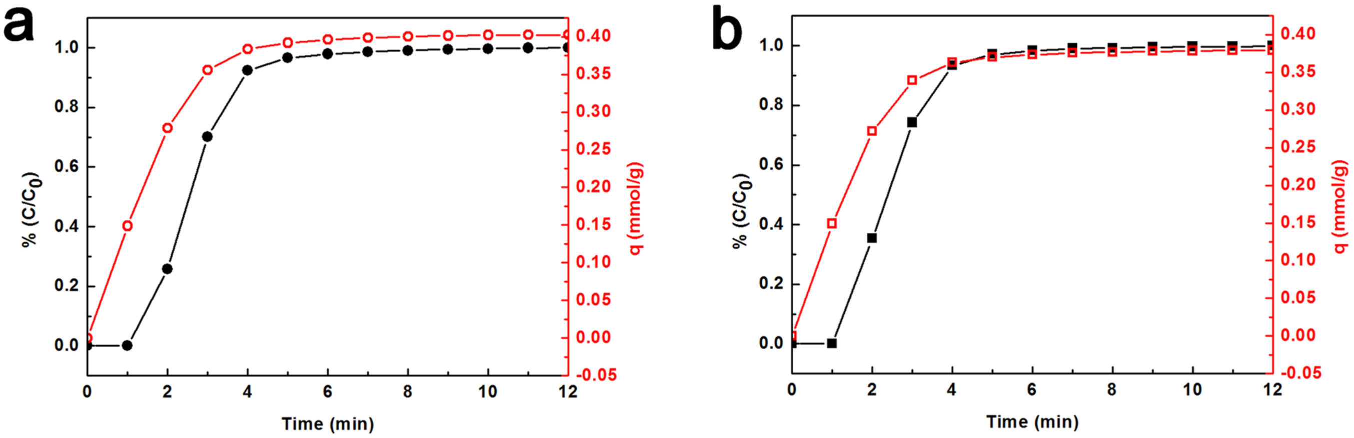

Figure 7. CO_2 adsorption kinetics of (a) meso-SiO_2−P[VBTMA][BF_4] and (b) meso-SiO_2−P[VBTMA][PF_6].

Morphology of Mesoporous Nanocomposites. The morphologies and dispersions of meso-SiO_2−Br, meso-SiO_2−P[VBTMA][BF_4], and meso-SiO_2−P[VBTMA][PF_6] were observed by SEM (Figure 6). Marked differences in the particle sizes of meso-SiO_2−Br particles, meso-SiO_2−P-[VBTMA][BF_4] nanocomposite, and meso-SiO_2−P[VBTMA]-[PF_6] nanocomposite were found. With the poly(ionic liquid)s grafting onto the surface of meso-silica, the particle size increased, whereas the dispersion state seemed to remain basically the same. Because of the high surface energy of SiO_2, the composites aggregated together. These differences in morphology are expected to lead to different performance characteristics, including different CO_2 capture capacities.

CO_2 Capture Capacity. The adsorption capacity of an adsorbent for CO_2 can be calculated as

$$q = \frac{1}{M}\left[\int_0^t Q\frac{C_0 - C}{1 - C}\,dt\right]\frac{T_0}{T}\frac{1}{V_m} \qquad (1)$$

where q is the adsorption capacity of the adsorbent for CO_2 ($mmol\cdot g^{-1}$); M is the mass of adsorbent (g); Q is the gas flow rate ($mL\cdot min^{-1}$); C_0 and C are the influent and effluent CO_2 volume concentrations, respectively (%); t represents the time (min); T_0 is 273.15 K; T represents the gas temperature (K); and V_m is 22.4 $mL\cdot mmol^{-1}$.

The CO_2 adsorption kinetics of the nanocomposites are shown in Figure 7. The two adsorbents can reach adsorption equilibrium quickly in about 5 min. They take up 0.4025 and 0.3793 mmol of CO_2 per gram, respectively, based on an average of three measured results at equilibrium, as calculated using eq 1. According to Tang et al.'s work on the adsorption capacity shown as mole percentages of monomer units,[20] the CO_2 sorption capacities of P[VBTMA][BF_4] and P[VBTMA]-[PF_6] involved in the nanocomposites were 0.3884 and 0.3323 $mmol\cdot g^{-1}$, respectively. To some extent, these results show the advantage of poly(ionic liquid)-based nanocomposites. Although the data on the advantage of nanocomposites are not obvious, this might be the result of the method utilized in the work. In this work, we assumed that the degree of polymerization from meso-silicon initiator in nanocomposites was the same as that for the pure poly(ionic liquid)s initiated by TMS-labeled initiator. Actually, because of the steric hindrance effect of SiO_2, the reaction rates might differ from each other, with the polymerization of monomer using the TMS-labeled initiator proceeding faster than that of the monomer grafted on the meso-SiO_2, as confirmed by our group through a simulation study.[43] Thus, the effective sorption part in the nanocomposites would be less than that in pure poly(ionic liquid)s. Even so, the results still showed that the nanocomposites had better sorption abilities. The improvements should result from the introduction of meso-silica into the nanocomposites. Although both the core and the shell of the nanocomposites have certain capacities, some pores will inevitably be filled by polymer chains, and thus, the capacity of the nanocomposites will be lower than the sum of the capacities of the two single components.

The adsorption isotherms of meso-SiO_2−P[VBTMA][BF_4] and meso-SiO_2−P[VBTMA][PF_6] at various CO_2 pressures and 30 °C are shown in Figure 8. Obviously, q increases as the pressure increases. Although the adsorption isotherm of meso-SiO_2−P[VBTMA][BF_4] appears to be nonlinear, that of meso-SiO_2−P[VBTMA][PF_6] is almost linear. The Henry's constant can be calculated as

$$H_i = \lim_{x_i \to 0} \frac{P_i}{x_i} \qquad (2)$$

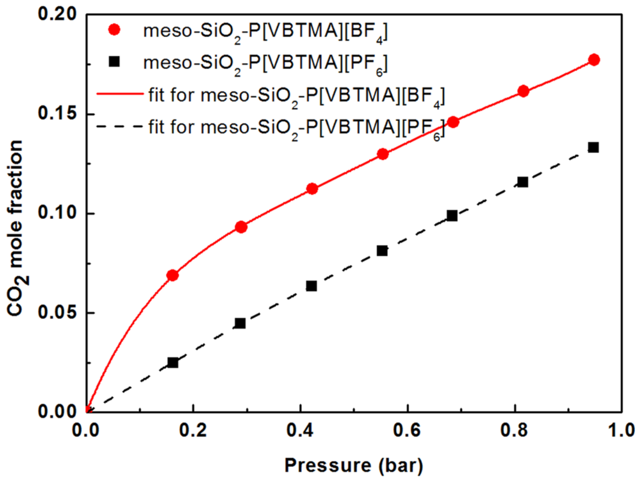

Figure 8. Isothermal adsorption of CO_2 by meso-SiO_2–P[VBTMA][BF_4] and meso-SiO_2–P[VBTMA][PF_6] at different pressures.

where H_i is the Henry's constant, x_i is the mole fraction of gas in the adsorbent, and P_i is the CO_2 pressure.

Because of the nonlinearity of x_i versus P_i throughout the whole pressure range, one can fit the data and extrapolate the slope to zero CO_2 partial pressure when calculating H_i.[44] The computed H_i values at 30 °C are 2.35 and 6.48 bar for meso-SiO_2–P[VBTMA][BF_4] and meso-SiO_2–P[VBTMA][PF_6], respectively, which are at the same level as those of ammonium-based poly(ionic liquid)s at 295 K.[21]

Factors Influencing CO_2 Capture Capacity. In consideration of the advantage of meso-SiO_2–P[VBTMA][BF_4] in CO_2 capture and experimental efficiency, we examined the dynamic adsorption process to obtain the adsorption data and trend. As shown in Figure 9, the core consisting of silica, the shell consisting of poly(ionic liquid), the presence of water vapor, and the test temperature all had an impact on the capacity of the nanocomposite adsorbents. From Figure 9a, one can see that the mesoporous silica core endows the mesoporous nanocomposite with a higher capacity than common nanocomposites, which also testifies to the existence of porous structures. The stereostructure and high surface area of mesosilica supply the high grafting density of the nanocomposite and are also beneficial for the diffusion of CO_2 into the nanocomposites.[45] Additionally, mesoporous nanocomposites with different shells result in different capacities, according to Figure 9b. We surmise that the difference is caused by the different anion diameters and their physical and chemical properties. The presence of water vapor can improve the CO_2 capture capacity, as shown in Figure 9c, which can be explained by the partial production of bicarbonate during CO_2 adsorption

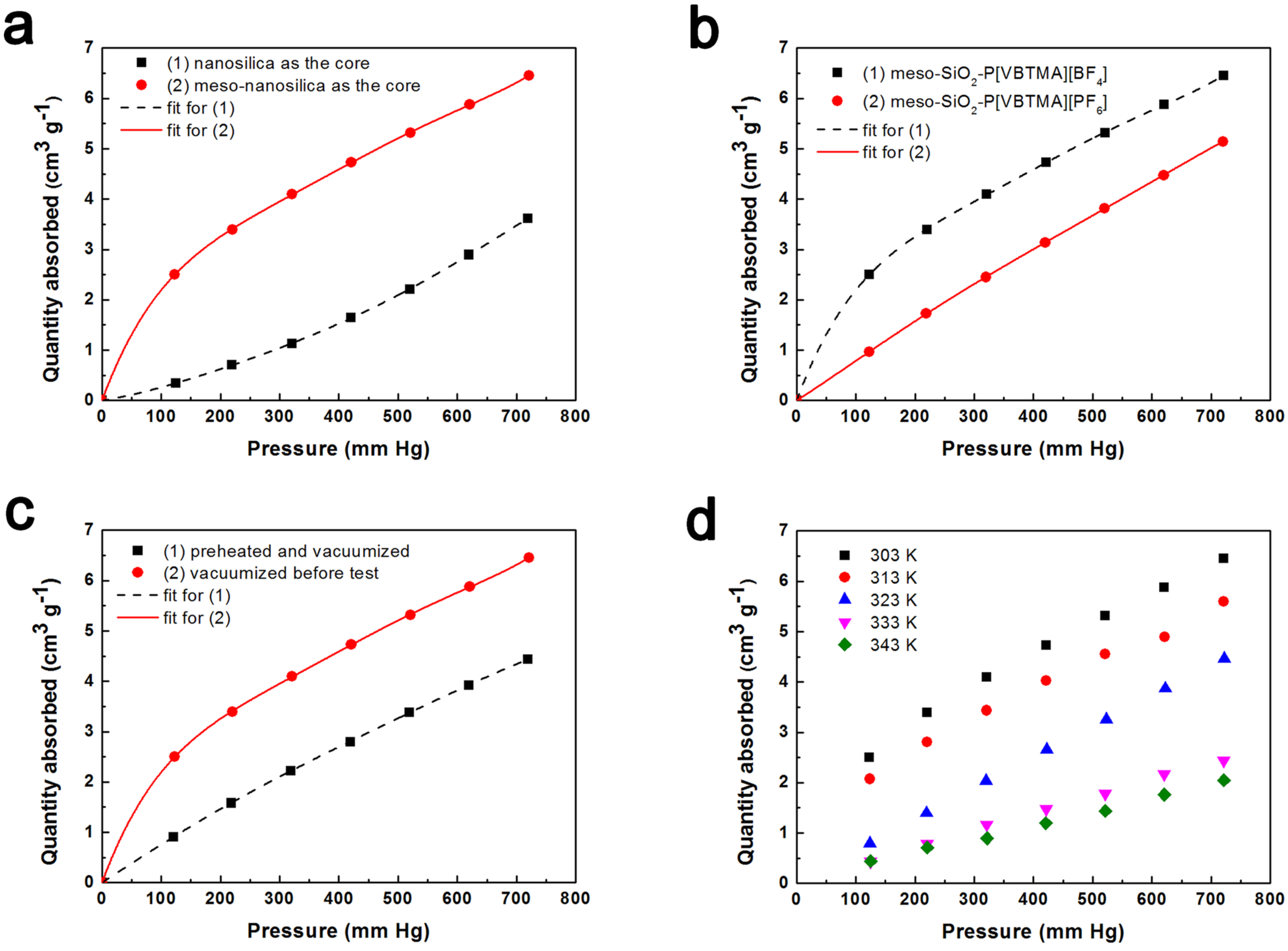

Figure 9. CO_2 adsorption in nanocomposites with different (a) cores, (b) shells, and (c) pretreatments and (d) CO_2 adsorption data of meso-SiO_2–P[VBTMA][BF_4] at different temperatures.

DOI: 10.1021/ie505014h
Ind. Eng. Chem. Res. 2015, 54, 3107–3115

on nanocomposites with hydrophilic ionic liquid monomers ([VBTMA][BF_4]) under humid conditions. However, the increase of q is not evident at the beginning, which might be because the residence time is so short that the bicarbonate formation reaction could not reach equilibrium. The dry adsorbent has a real capacity, whereas the wet adsorbent shows an apparent sorption quantity that is higher than the former. Finally, the impact of pressure was investigated. As shown in Figure 9d, at a certain temperature, the capacity increased as the pressure increased. In contrast, at a certain pressure, the capacity decreased as the temperature increased, because adsorption is an exothermic process, so it is not beneficial to perform absorption at high temperatures, and also, the movement of molecules becomes vigorous, which is not good for the adsorption process. The equilibrium times for the five selected temperatures were almost the same, indicating that the temperature influences the capacity, but not the equilibrium time. The above data show that low temperatures are preferable for the use of the nanocomposites prepared in this work.

As a whole, the above data and analysis can provide a possible explanation for the adsorption phenomenon: Absorption (occurring in the bulk) and adsorption (occurring at the surface) both take place during CO_2 adsorption on the polymer shell.[20] Subsequently, because of the driving force of a concentration difference, CO_2 diffuses into the pores of the meo-silica core, causing secondary adsorption. The CO_2 adsorption cycle of meso-SiO_2−P[VBTMA][BF_4] is shown in Figure 10. By comparing the different cycles, it can be seen that irreversible chemical absorption occurs during the sorption process, which leads to a capacity decrease at the second cycle. However, the main process is still physical adsorption, which enables the material to be used repeatedly. In addition, for the purpose of improving the adsorption capacity of the polymers, it is important to avoid filling polymers into the pores of the meso-silica.

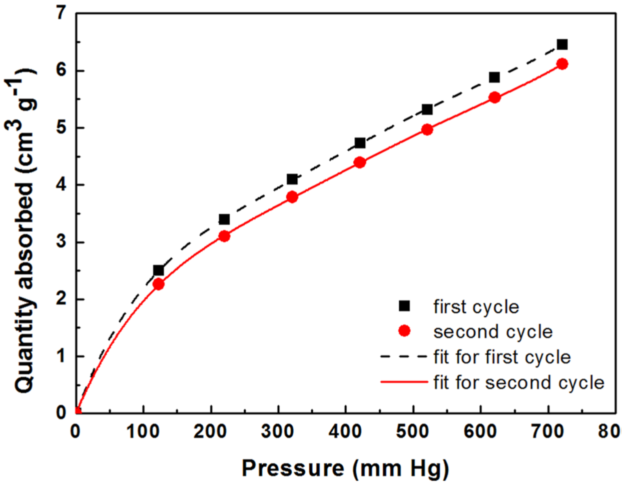

Figure 10. CO_2 adsorption cycle of meso-SiO_2−P[VBTMA][BF_4].

■ CONCLUSIONS

Two nanocomposite absorbents, namely, meso-SiO_2−P-[VBTMA][BF_4] and meso-SiO_2−P[VBTMA][PF_6], were synthesized by SI-ATRP using mesoporous nanosilica as the initiator. Their CO_2 adsorption behaviors were investigated under different conditions. The adsorbents were still porous and had reasonably high surface areas after ionic liquid monomer had been grafted onto the meso-silica; therefore, they could adsorb CO_2 rapidly and show outstanding adsorption capacities and selectivities, as well as repeatability. At 30 °C, meso-SiO_2−P[VBTMA][BF_4] had the highest CO_2 absorption capacity of 0.4025 mmol g^{-1}, whereas meso-SiO_2−P[VBTMA][PF_6] showed the highest CO_2 absorption capacity of 0.3793 mmol g^{-1} for a simulated flue gas containing 10 vol % CO_2. Compared with pure poly(ionic liquid)s, the presence of the meso-silica core does enhance the CO_2 capture capacity. The presence of water vapor can strengthen the CO_2 capture capacity, which is why meso-SiO_2−P[VBTMA][BF_4] with a hydrophilic shell was found to have a higher capacity than meso-SiO_2−P[VBTMA][PF_6]. Increasing the test temperature inhibited the CO_2 capture capacity, which implies that low temperatures are preferable for the use of the nanocomposites. Overall, the introduction of meso-silica not only increases the capacity of the polymer but also decreases the cost, which is promising for applications in CO_2 capture.

■ AUTHOR INFORMATION

Corresponding Author

*E-mail: luozh@sjtu.edu.cn. Tel.: +86-21-54745602. Fax: +86-21-54745602.

Author Contributions

‡H.C. and P.W. contributed equally to this work.

Notes

The authors declare no competing financial interest.

■ ACKNOWLEDGMENTS

The authors thank the National Natural Science Foundation of China (No. 21276213), the Research Fund for the Doctoral Program of Higher Education (No. 20130073110077), and the National High Technology Research and Development Program of China (No. 2013AA032302) for supporting this work. H.C. also acknowledges the Natural Science Research Project of Anhui Province (Nos. 1308085MB23 and 1408085MB30) and the Research Project of Hefei Normal University (No. 2013syq01). Financial support from the Exploratory Bilateral Co-Operation Programme SJTU-KU Leuven 2013-2014 (BOF-ISP) is acknowledged. J.L. acknowledges the Research Foundation-Flanders (FWO) for a postdoctoral fellowship.

■ REFERENCES

(1) Satyapal, S.; Filburn, T.; Trela, J.; Strange, J. Performance and Properties of a Solid Amine Sorbent for Carbon Dioxide Removal in Space Life Support Applications. *Energy Fuels* **2001**, *15*, 250−255.

(2) Hwang, H. T.; Harale, A. P.; Liu, K. T.; Sahimi, M.; Tsotsis, T. T. A membrane-based reactive separation system for CO_2 removal in a life support system. *J. Membr. Sci.* **2008**, *315*, 116−124.

(3) Cavenati, S. C.; Grande, A.; Rodrigues, A. E. Adsorption Equilibrium of Methane, Carbon Dioxide, and Nitrogen on Zeolite 13X at High Pressures. *J. Chem. Eng. Data* **2004**, *49*, 1095−1101.

(4) Delgado, J. A.; Uguina, M. A.; Sotelo, J. L.; Ruiz, B.; Rosario, M. R. Separation of carbon dioxide/methane mixtures by adsorption on a basic resin. *Adsorption* **2007**, *13*, 373−383.

(5) Peng, Y.; Li, Y.; Ban, Y.; Jin, H.; Jiao, W.; Liu, X.; Yang, W. Metal−organic framework nanosheets as building blocks for molecular sieving membranes. *Science* **2014**, *346*, 1356−1359.

(6) Meng, J. Q.; Yuan, J. Y.; Kang, L.; Zhang, Y. F.; Du, Q. Y. Surface glycosylation of polysulfone membrane towards a novel complexing membrane for boron removal. *J. Colloid Interface Sci.* **2012**, *368*, 197−207.

(7) Luo, J.; Conrad, O.; Vankelecom, I. F. J. Imidazolium methanesulfonate as a high temperature proton conductor. *J. Mater. Chem. A* **2013**, *1*, 2238−2247.

(8) Luo, J.; Conrad, O.; Vankelecom, I. F. J. Physicochemical properties of phosphonium-based and ammonium-based protic ionic liquids. *J. Mater. Chem.* **2012**, *22*, 20574−20579.

(9) Blanchard, L. A.; Hancu, D.; Beckman, E. J.; Brennecke, J. F. Green processing using ionic liquids and CO_2. *Nature* **1999**, *399*, 28−29.

(10) Blanchard, L. A.; Gu, Z. Y.; Brennecke, J. F. High-Pressure Phase Behavior of Ionic Liquid/CO_2 Systems. *J. Phys. Chem. B* **2001**, *105*, 2437−2444.

(11) Cadena, C.; Anthony, J. L.; Shah, J. K.; Morrow, T. I.; Brennecke, J. F.; Maginn, E. Why Is CO_2 So Soluble in Imidazolium-Based Ionic Liquids? *J. Am. Chem. Soc.* **2004**, *126*, 5300−5308.

(12) Scovazzo, P.; Camper, D.; Kieft, J.; Poshusta, J.; Koval, C.; Noble, R. D. Regular Solution Theory and CO_2 Gas Solubility in Room-Temperature Ionic Liquids. *Ind. Eng. Chem. Res.* **2004**, *43*, 6855−6860.

(13) Bates, E. D.; Mayton, R. D.; Ntai, I.; David, J. H. CO_2 Capture by a Task-Specific Ionic Liquid. *J. Am. Chem. Soc.* **2002**, *124*, 926−927.

(14) Fortunato, R.; Afonso, C. A. M.; Reis, M. A. M.; Crespo, J. G. Supported liquid membranes using ionic liquids: Study of stability and transport mechanisms. *J. Membr. Sci.* **2004**, *242*, 197−209.

(15) Yuan, J. Y.; Antonietti, M. Poly(ionic liquid)s: Polymers expanding classical property profiles. *Polymer* **2011**, *52*, 1469−1482.

(16) Mecerreyes, D. Polymeric ionic liquids: Broadening the properties and applications of polyelectrolytes. *Prog. Polym. Sci.* **2011**, *36*, 1629−1648.

(17) Yu, B.; Zhou, F.; Wang, C. W.; Liu, W. M. A novel gel polymer electrolyte based on poly ionic liquid 1-ethyl 3-(2-methacryloyloxy ethyl) imidazolium iodide. *Eur. Polym. J.* **2007**, *43*, 2699−2707.

(18) Matsumoto, K.; Endo, T. Synthesis of Ion Conductive Networked Polymers Based on an Ionic Liquid Epoxide Having a Quaternary Ammonium Salt Structure. *Macromolecules* **2009**, *42*, 4580−4584.

(19) Zhang, Z. M.; Wu, L. B.; Dong, J.; Li, B. G.; Zhu, S. P. Preparation and SO_2 Sorption/Desorption Behavior of an Ionic Liquid Supported on Porous Silica Particles. *Ind. Eng. Chem. Res.* **2009**, *48*, 2142−2148.

(20) Tang, J. B.; Tang, H. D.; Sun, W. L.; Radosz, M.; Shen, Y. Q. Low-pressure CO_2 sorption in ammonium-based poly(ionic liquid)s. *Polymer* **2005**, *46*, 12460−12467.

(21) Tang, J. B.; Tang, H. D.; Sun, W. L.; Radosz, M.; Shen, Y. Q. Poly(ionic liquid)s as new materials for CO_2 absorption. *J. Polym. Sci. A: Polym. Chem.* **2005**, *43*, 5477−5489.

(22) Tang, J. B.; Tang, H. D.; Sun, W. L.; Radosz, M.; Shen, Y. Q. Poly(ionic liquid)s: A new material with enhanced and fast CO_2 absorption. *Chem. Commun.* **2005**, *45*, 3325−3327.

(23) Quinn, R.; Laciak, D. V. Polyelectrolyte-salt blend membranes for acid gas separations. *J. Membr. Sci.* **1997**, *131*, 61−69.

(24) Quinn, R.; Laciak, D. V.; Pez, G. P. Polyelectrolyte membranes for acid gas separations. *Membr. Sci.* **1997**, *131*, 49−60.

(25) Quinn, R.; Laciak, D. V.; Appleby, B.; Pez, G. P. Polyelectrolyte membranes for the separation of acid gases. U.S. Patent 5,336,298, 1994.

(26) Quinn, R. A repair technique for acid gas selective polyelectrolyte membranes. *J. Membr. Sci.* **1998**, *139*, 97−102.

(27) Macedonia, M. D.; Moore, D. D.; Maginn, E. J. Adsorption Studies of Methane, Ethane, and Argon in the Zeolite Mordenite: Molecular Simulations and Experiments. *Langmuir* **2000**, *16*, 3823−3834.

(28) Ejaz, M.; Ohno, K.; Tsujii, Y.; Fukuda, T. Controlled Grafting of a Well- Defined Glycopolymer on a Solid Surface by Surface-Initiated Atom Transfer Radical Polymerization. *Macromolecules* **2000**, *33*, 2870−2874.

(29) Kim, J. B.; Huang, W.; Miller, D.; Baker, G. L.; Bruening, M. L. Kinetics of surface-initiated atom transfer radical polymerization. *J. Polym. Sci. A: Polym. Chem.* **2003**, *41*, 386−394.

(30) Matyjaszewski, K.; Miller, P. J.; Shukla, N.; Immaraporn, B.; Gelman, A.; Luokala, B. B.; Siclovan, T. M.; Kickelbick, G.; Vallant, T.; Hoffmann, H.; Pakula, Y. Polymers at Interfaces: Using Atom Transfer Radical Polymerization in the Controlled Growth of Homopolymers and Block Copolymers from Silicon Surfaces in the Absence of Untethered Sacrificial Initiator. *Macromolecules* **1999**, *32*, 8716−8724.

(31) Huang, W.; Kim, J. B.; Bruening, M. L.; Baker, G. L. Functionalization of Surfaces by Water-Accelerated Atom-Transfer Radical Polymerization of Hydroxyethyl Methacrylate and Subsequent Derivatization. *Macromolecules* **2002**, *35*, 1175−1179.

(32) Feng, W.; Brash, J.; Zhu, S. Atom-transfer radical grafting polymerization of 2-methacryloyloxyethyl phosphorylcholine from silicon wafer surfaces. *J. Polym. Sci. A: Polym. Chem.* **2004**, *42*, 2931−2942.

(33) Benetti, E. M.; Johannes, E. B.; Zapotoczny, S.; Textor, M.; Vansco, G. J. Poly(methacrylic acid) Grafts Grown from Designer Surfaces: The Effect of Initiator Coverage on Polymerization Kinetics, Morphology, and Properties. *Macromolecules* **2009**, *42*, 1640−1647.

(34) Edmondson, S.; Vo, C. D.; Armes, S. P.; Unali, G. F. Surface Polymerization from Planar Surfaces by Atom Transfer Radical Polymerization Using Polyelectrolytic Macroinitiators. *Macromolecules* **2007**, *40*, 5271−5278.

(35) Feng, W.; Chen, R.; Brash, J. L.; Zhu, S. Surface-Initiated Atom Transfer Radical Polymerization of Oligo(ethylene glycol) Methacrylate: Effect of Solvent on Graft Density. *Macromol. Rapid Commun.* **2005**, *26*, 1383−1388.

(36) Matyjaszewski, K.; Dong, H.; Jakubowski, W.; Pietrasik, J.; Kusumo, A. Grafting from Surfaces for "Everyone": ARGET ATRP in the Presence of Air. *Langmuir* **2007**, *23*, 4528−4531.

(37) Sheiko, S. S.; Sumerlin, B. S.; Matyjaszewski, K. Cylindrical molecular brushes: Synthesis, characterization, and properties. *Prog. Polym. Sci.* **2008**, *33*, 759−785.

(38) Ohno, K.; Kayama, Y.; Ladmiral, V.; Fukuda, T.; Tsujii, Y. A Versatile Method of Initiator Fixation for Surface-Initiated Living Radical Polymerization on Polymeric Substrates. *Macromolecules* **2010**, *43*, 5569−5574.

(39) Lego, B.; Skene, W. G.; Giasson, S. Swelling Study of Responsive Poly electro- lyte Brushes Grafted from Mica Substrates: Effect of pH, Salt, and Grafting Density. *Macromolecules* **2010**, *43*, 4384−4393.

(40) Borozenko, O.; Godin, R.; Lau, K. L.; Mah, W.; Cosa, G.; Skene, W. G.; Giasson, S. Monitoring in Real-Time the Degrafting of Covalently Attached Fluorescent Polymer Brushes Grafted to Silica Substrates—Effects of pH and Salt. *Macromolecules* **2011**, *44*, 8177−8184.

(41) Gao, X.; Feng, W.; Zhu, S.; Heather, S.; Brash, J. L. Kinetic Modeling of Surface-Initiated Atom Transfer Radical Polymerization. *Macromol. React. Eng.* **2010**, *4*, 235−250.

(42) Wang, P.; Zhou, Y. N.; Luo, J. S.; Luo, Z. H. Poly(ionic liquid)s-based nanocomposite polyelectrolytes with tunable ionic conductivity prepared *via* SI-ATRP. *Polym. Chem.* **2014**, *5*, 882−891.

(43) Zhou, Y. N.; Luo, Z. H. Insight into the ATRP rate controlling ability of initiator structure: Micromolecular, macromolecular, and immobilized initiators. *J. Polym. Sci. A: Polym. Chem.* **2014**, *52*, 2228−2238.

(44) Anthony, J. L.; Maginn, E. J.; Brennecke, J. F. Solubilities and Thermodynamic Properties of Gases in the Ionic Liquid 1-*n*-Butyl-3-methylimidazolium Hexafluorophosphate. *J. Phys. Chem. B* **2002**, *106*, 7315−7320.

(45) Wang, X. F.; Akhmedov, N. G.; Duan, Y. H.; Luebke, D.; Hopkinson, D.; Li, B. Y. Amino acid-functionalized ionic liquid solid sorbents for post-combustion carbon capture. *ACS Appl. Mater. Interfaces* **2013**, *5*, 8670−8677.